A measurement of the $z = 0$ UV background from Hα fluorescence

Michele Fumagalli,[1,2]★ Francesco Haardt,[3,4] Tom Theuns,[1] Simon L. Morris,[2]
Sebastiano Cantalupo,[5] Piero Madau[6] and Matteo Fossati[7,8]

[1]*Institute for Computational Cosmology, Durham University, South Road, Durham DH1 3LE, UK*
[2]*Centre for Extragalactic Astronomy, Durham University, South Road, Durham DH1 3LE, UK*
[3]*DiSAT, Università degli Studi dell'Insubria, Via Valleggio 11, I-22100 Como, Italy*
[4]*INFN, Sezione di Milano-Bicocca, Piazza della Scienza 3, I-20126 Milano, Italy*
[5]*Institute for Astronomy, ETH Zurich, Wolfgang-Pauli-Strasse 27, CH-8093 Zurich, Switzerland*
[6]*Department of Astronomy & Astrophysics, University of California, 1156 High Street, Santa Cruz, CA 95064, USA*
[7]*Universitäts-Sternwarte München, Scheinerstrasse 1, D-81679 München, Germany*
[8]*Max-Planck-Institut für Extraterrestrische Physik, Giessenbachstrasse, D-85748 Garching, Germany*

ABSTRACT

We report the detection of extended Hα emission from the tip of the H I disc of the nearby edge-on galaxy UGC 7321, observed with the Multi Unit Spectroscopic Explorer (MUSE) instrument at the Very Large Telescope. The Hα surface brightness fades rapidly where the H I column density drops below $N_{\rm H I} \sim 10^{19}$ cm^{-2}, consistent with fluorescence arising at the ionization front from gas that is photoionized by the extragalactic ultraviolet background (UVB). The surface brightness measured at this location is $(1.2 \pm 0.5) \times 10^{-19}$ erg s^{-1} cm^{-2} arcsec^{-2}, where the error is mostly systematic and results from the proximity of the signal to the edge of the MUSE field of view, and from the presence of a sky line next to the redshifted Hα wavelength. By combining the Hα and the H I 21 cm maps with a radiative transfer calculation of an exponential disc illuminated by the UVB, we derive a value for the H I photoionization rate of $\Gamma_{\rm H I} \sim (6\text{–}8) \times 10^{-14}$ s^{-1}. This value is consistent with transmission statistics of the Lyα forest and with recent models of a UVB that is dominated by quasars.

Key words: radiative transfer – techniques: imaging spectroscopy – galaxies: individual: UGC 7321 – diffuse radiation – ultraviolet: general.

1 INTRODUCTION

Massive stars and active galactic nuclei (AGNs) in galaxies produce copious amounts of ultraviolet (UV) radiation. A fraction of these UV photons escape from the interstellar medium (ISM) of the host galaxy into the intergalactic medium (IGM), building up an extragalactic UV background (UVB). Following reionization, this UVB keeps the bulk of the IGM ionized (e.g. Gunn & Peterson 1965; Bolton & Haehnelt 2007), regulates its temperature (e.g. Theuns et al. 2002) and sets a characteristic virial temperature below which haloes do not form galaxies (e.g. Okamoto, Gao & Theuns 2008). The UVB is therefore an important ingredient in models of galaxy formation. Moreover, the UVB encodes the cumulative history of star formation and AGN activity, and depends on the redshift and luminosity-dependent escape fractions of galaxies (e.g. Haardt & Madau 1996). A detailed understanding of the time evolution of the spectral shape and intensity of the UVB [hereafter $J_\nu(z)$] is of critical importance in many areas of astrophysics.

The amplitude of the UVB at redshifts $z \sim 2$–3 is expected to be more than 10 times the present-day value (Haardt & Madau 2012), and three methods have been used to attempt to measure J_ν at these redshifts. First, a background of H I ionizing photons will result in recombination radiation, such as Lyα, when such photons impinge on optically thick H I clouds (e.g. Gould & Weinberg 1996; Cantalupo et al. 2005). However, searches for this Lyα 'fluorescence' have remained inconclusive (e.g. Bunker, Marleau & Graham 1998; Rauch et al. 2008). The expected intrinsic surface brightness (SB) is low, and the signal is furthermore significantly lowered by cosmological redshifting, making this measurement very challenging. Secondly, J_ν can be constrained by determining out to which distance a luminous source, such as a quasar, outshines the UVB, via the so-called proximity effect (e.g. Murdoch et al. 1986; Bajtlik, Duncan & Ostriker 1988; Rollinde et al. 2005). However, the value inferred for J_ν depends on other properties of the system that are difficult to constrain, such as the time-dependence of the luminosity of the source, and the temperature and density structure of its surrounding medium (Faucher-Giguère et al. 2008a; Prochaska et al. 2013). Thirdly, constraints on J_ν can be derived by comparing the observed transmission statistics of the Lyα forest to those

★ E-mail: michele.fumagalli@durham.ac.uk

measured in hydrodynamic simulations (e.g. Rauch et al. 1997). This method, which currently offers the primary constraints on J_ν, suffers from systematic uncertainties, because the transmission statistics also depend on the relatively poorly known temperature–density relation of the photoionized IGM (e.g. Bolton et al. 2005; Faucher-Giguère et al. 2008b; Becker & Bolton 2013).

In the low-redshift Universe, at $z \lesssim 1$, Lyα transmission statistics also provide the best current constraints on J_ν (e.g. Kollmeier et al. 2014; Khaire & Srianand 2015; Shull et al. 2015; Viel et al. 2016), but observing the Lyα forest requires UV-spectroscopy from space. The detection of Lyα fluorescence is challenging because the amplitude of the UVB is low and the IGM is more diffuse at these redshifts when compared to $z \sim 2$–3. Interestingly, fluorescence could also be detected in Hα, by observing the ionization front of neutral H I clouds photoionized by the UVB (Vogel et al. 1995; Donahue, Aldering & Stocke 1995; Weymann et al. 2001), or in the outskirts of the H I discs of galaxies (e.g. Maloney 1993; Dove & Shull 1994; Bland-Hawthorn, Freeman & Quinn 1997; Ćirković, Bland-Hawthorn & Samurović 1999; Madsen et al. 2001). Using this technique, Adams et al. (2011) targeted the nearby edge-on galaxy UGC 7321, obtaining an upper limit on $\Gamma_{H I}$, which is the H I photoionization rate of the UVB.[1] The same group also reported a detection,[2] which has not been published at the time of writing (see Uson et al. 2012).

In the absence of firm observational constraints on J_ν, the current parametrization of the UVB relies mostly on radiative transfer calculations that follow the build-up of the UVB accounting for sources and sinks of radiation. These models have input parameters that are difficult to measure, such as the emissivity and escape fraction of ionizing photons from massive stars and AGNs in galaxies, and the distribution of H I absorbers (Haardt & Madau 1996; Shull et al. 1999; Faucher-Giguère et al. 2009; Haardt & Madau 2012). Therefore, different models predict values of $\Gamma_{H I}$ that differ by factors of a few, primarily because the observational data that enter the modelling are not well known. Such a relatively large uncertainty in $\Gamma_{H I}$ then impacts the reliability of other predictions, for example the outcome of cosmological hydrodynamic simulations (see e.g. Kollmeier et al. 2014; Oñorbe, Hennawi & Lukić 2016). For example, Kollmeier et al. (2014) argue that the value of J_ν predicted by Haardt & Madau (2012) underestimates the UVB at $z \sim 0$ by a factor up to 5 compared to what is required by the transmission statistics of the low-redshift Lyα forest. Follow-up work confirms this discrepancy, although revising downward its severity (e.g. Khaire & Srianand 2015; Shull et al. 2015; Viel et al. 2016).

In this paper, we describe the results from new observations designed to measure J_ν through the experiment proposed by Adams et al. (2011), who attempted to measure the UVB intensity by searching for the Hα recombination line arising from gas that is photoionized by the UVB at the edge of the H I disc in the nearby spiral galaxy UGC 7321. The distance to this galaxy is $\sim$10 Mpc and it has a mostly unperturbed H I disc seen edge-on, thus providing the ideal conditions for measuring the Hα fluorescence induced by the UVB. A critical breakthrough enabling this experiment is the deployment of the Multi Unit Spectroscopic Explorer (MUSE; Bacon et al. 2010) at the Very Large Telescope (VLT), which offers

a powerful combination of a relatively large field of view (FOV; 1×1 arcmin^2) and high throughput ($\sim$35 per cent at $\lambda \sim 6600$ Å). Indeed, the capability to combine the large collecting area of VLT with an integral field spectrograph allows observers to create composites of $\gtrsim$10 000 independent spectra, thus increasing by a factor of $\gtrsim$100 the sensitivity achievable with traditional long-slit spectrographs (e.g. Rauch et al. 2008).

Here, we present results from a pilot MUSE observation, reporting a detection of extended Hα emission at the location of the ionization front inferred from photoionization models for UGC 7321. The layout of this paper is as follows. In Section 2, we describe the new observations and the reduction techniques, followed by the analysis of the data in Section 3. In Section 4, we present updated photoionization modelling of UGC 7321, through which we constrain the intensity of the UVB at $z \sim 0$. We summarize our results in Section 5, concluding with a discussion of how future observations can refine the measurement of the UVB intensity.

2 OBSERVATIONS AND DATA REDUCTION

MUSE observations of UGC 7321 have been acquired as part of the programme ID 095.A-0090 (PI Fumagalli) between 2015 June and 2016 January at the UT4 VLT. All observations have been completed in dark time, under clear or photometric conditions, with seeing $\lesssim$1.5 arcsec and airmass $<$1.6. For these observations, we used the MUSE Wide Field Mode with slow guiding. A total of 14 exposures of 1465 s each, totalling 5.7 h on target, were acquired at the position α(J2000) = 12:17:15.3 and δ(J2000) = +22:31:16.9 with small offsets and 90° rotations in between exposures. Fig. 1 shows an RGB image of UGC 7321 with the position of the MUSE FOV and H I contours from Adams et al. (2011, see also Uson & Matthews 2003). The location of the pointing was chosen to overlap with the region where the SB was expected to be maximal according to the model of Adams et al. (2011), while sampling a mostly blank sky region in the bottom part of the FOV as well (see Fig. 2).

Individual exposures have been reduced using the ESO MUSE pipeline (v1.6.2; Weilbacher et al. 2014) that applies standard calibrations to the raw data, including bias subtraction, flat-fielding, flux and wavelength calibrations, and baryocentric corrections.

After the individual exposures have been processed with basic reduction techniques, we produce three final data sets for the subsequent analysis using (i) the ESO pipeline; (ii) the CUBEXTRACTOR package (CUBEX; Cantalupo, in preparation) following the procedures described in Borisova et al. (2016) and Fumagalli et al. (2016) and (iii) a custom PYTHON post-processing pipeline and the Zurich Atmosphere Purge (ZAP) package (Soto et al. 2016). Each of these three methods applies independent algorithms for the sky subtraction and, in some cases, for additional illumination corrections, allowing us to further test the robustness of our results with respect to different reduction techniques.

In the following, fluxes recorded in the data cubes are converted into SB units using the pixel size of 0.2×0.2 arcsec^2. We also apply a correction for Galactic extinction in the direction of UGC 7321, which we estimate to be $f_{dust} = 1.06 \pm 0.01$ from the Milky Way dust map (Schlafly & Finkbeiner 2011). As described in Adams et al. (2011), the internal extinction of UGC 7321 is believed to have negligible effects at the location of our observations, and it is not considered further. The distance to UGC 7321 is somewhat uncertain, with values reported in the literature ranging from $\sim$4 to 23 Mpc. We follow Uson & Matthews (2003) and Adams et al. (2011) in this work and assume a distance of $D_{gal} = 10$ Mpc, with a corresponding angular scale of $\alpha = 48.5$ pc arcsec^{-1}. We note,

---

[1] The photoionization rate is $\Gamma_{H I} = \int_{\nu_0}^{\infty} (4\pi J_\nu / h\nu)\, \sigma_{H I}(\nu)\, d\nu$, where $\sigma_{H I}$ is the photoionization cross-section and ν_0 is the frequency corresponding to the ionization potential of hydrogen.

[2] The announcement of this result is also available at http://iactalks.iac.es/talks/view/393.
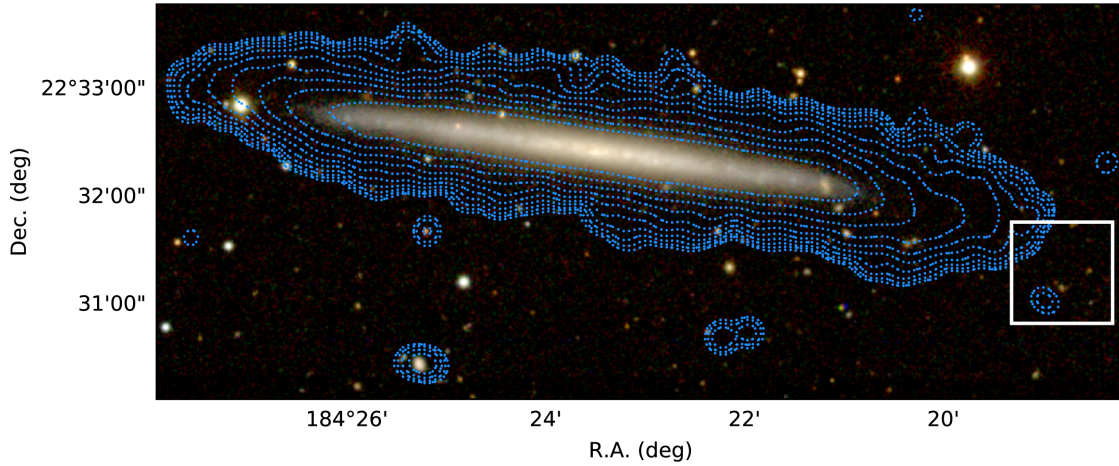
Figure 1. False-colour RGB image of UGC 7321 from SDSS imaging (*gri*), with H I column-density contours from Adams et al. (2011) in steps of $(1.0, 1.9, 3.6, 6.7, 12.6, 23.8, 44.8, 84.5) \times 10^{19}\ \mathrm{cm}^{-2}$ for the outermost eight contours. The position of the MUSE FOV is shown in white.

however, that our results are based on distance-independent quantities, such as SB and relative separations in the plane of the sky.

2.1 ESO data product

For the preparation of the first data set (hereafter the ESO data cube), we perform sky subtraction on the individual exposures using the `muse_scipost` recipe provided within the ESO pipeline. This procedure subtracts a sky model from the data, correcting for local variation of the line spread function (LSF) in an attempt to minimize the residuals of bright sky lines. The sky continuum level is computed internally, by selecting a range of pixels with low illumination to avoid the presence of sources.

Following sky subtraction, we align all the exposures relative to each other by using continuum-detected sources as reference. Subsequently, we reconstruct a final data cube using the `muse_exp_combine` recipe that resamples data on a regular cube of 1.25 Å in the spectral directions, and 0.2 arcsec in the two spatial directions. As a last step, we correct the absolute astrometric solution using the Sloan Digital Sky Survey (SDSS) imaging as reference system (Alam et al. 2015). We further test the quality of the flux calibration against SDSS using galaxies in the field finding good agreement (within ∼15 per cent).

Inspection of the final data cube reveals the presence of sky residuals with amplitude comparable to the signal we wish to detect. For this reason, we will only use the ESO product as a reference grid for computing the astrometric and wavelength solution during the reconstruction of new data cubes that are post-processed with additional software as described in the following sections.

2.2 CUBEX data product

The second data set (hereafter the CUBEX data cube) is prepared using a combination of procedures distributed as part of the CUBEX package (Cantalupo, in preparation). At first, we reconstruct a re-sampled data cube for each exposure, after it has been processed for basic calibrations using the ESO pipeline. At this stage, sky subtraction has not been performed, and we use the ESO data cube as a common reference frame for the final astrometric solution of individual exposures. All the subsequent post-processing techniques are applied to these reconstructed data cubes, thus avoiding multiple interpolations of the data.

The next step uses the `CubeFix` procedure to minimize the residual illumination differences that are not fully corrected by flat-fields across the 24 integral field units (IFUs) that compose the MUSE instrument. This correction is achieved by using both the sky lines and the continuum sky emission to rescale slices[3] relative to each others, also accounting for wavelength-dependent variations. This step ensures that residual differences in illumination across the field are removed, achieving a uniformity of better than ∼0.1 per cent of the sky level on average (Borisova et al. 2016). After this correction, the sky is subtracted from the resampled cubes using the flux-conserving `CubeSharp` procedure, which is designed to minimize the residuals arising from variations in the LSF across different IFUs. The above steps are iterated twice using the products of the previous iteration to identify and mask astronomical sources within the cube. To minimize the risk of altering the astrophysical signal during sky subtraction, when computing the normalization of the sky flux as a function of wavelength with `CubeSharp`, we further mask the top half of the MUSE FOV, where the Hα signal is expected to lie (see Fig. 2). In the end, a final data cube is reconstructed by averaging individual exposures applying a 3σ-clipping algorithm.

2.3 ZAP data product

The preparation of the third data set (hereafter the ZAP data cube) follows a procedure similar to the one adopted for the CUBEX data cube, but using PYTHON code, we developed to perform the illumination correction and the ZAP package (Soto et al. 2016) to perform sky subtraction.

As done previously, we resample each exposure after basic reduction with the ESO pipeline on to a regular grid, using the ESO data cube as reference for the astrometry and wavelength grid. At this stage, we also produce masks that trace each voxel in the reconstructed cube back to the original MUSE IFU, retaining also information on the pixel location within stacks.[4] After masking continuum-detected sources, we use sky regions to map and correct

---

[3] In MUSE, a slice is the basic unit inside an IFU, and corresponds to a $0.2 \times 15\ \mathrm{arcsec}^2$ segment in the spatial direction.

[4] Within MUSE, a stack is a group of 12 slices within an IFU. A MUSE IFU contains four stacks of 12 slices each. A voxel is defined as a data point inside a cube, while a spaxel is a pixel in the spatial direction.
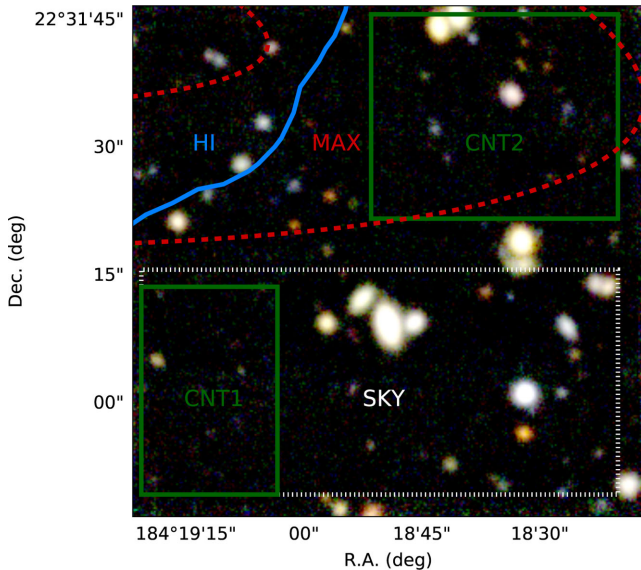
Figure 2. The MUSE FOV shown in a false-colour image obtained from three 1000 Å wide images reconstructed from the CUBEX data cube. The location of five regions that contain pixels used to generate deep stack spectra throughout our analysis are also displayed. These regions are defined in Section 2.4.

the residual illumination differences first across IFUs as a function of wavelength using coarse spectral bins of 100 Å, and then across stacks collapsing the entire cube into an image. These corrections are of the order of $\lesssim 1$ per cent and, by construction, they preserve the mean flux across the cube as a function of wavelength. We have verified that the photometric properties of sources detected across the field are preserved when compared to the ESO data cube. A major difference with CubeFix is that we do not correct slices individually and we do not separate the contribution of sky lines and sky continuum when computing the scaling factors.

After this step, we use the ZAP code to perform sky subtraction. As described in Soto et al. (2016), ZAP employs principal component analysis (PCA) to describe and subtract the sky emission within each MUSE voxel. As for the CUBEX product, we reduce the risk of subtracting astronomical signal by applying a mask in addition to the internal ZAP algorithms that minimize the inclusion of pixels with sources in the computation of the PCA components. To this end, we compute the sky eigenspectra using only pixels in the bottom half of the MUSE FOV, in a 'SKY region' (see Section 2.4 and Fig. 2) that does not overlap with the region where Hα is maximal in the model by Adams et al. (2011). Finally, we combine all the exposures into a mean data cube.

2.4 Definition of pixel regions

Throughout our analysis, we make extensive use of regions in the image plane to generate deep composite spectra. These regions are shown in Fig. 2, superimposed on a false-colour image of the MUSE FOV that we obtain from three 1000 Å wide images extracted from the CUBEX data cube.

These regions are defined as it follows. The first region, labelled 'H I', contains all the pixels within the H I column-density contour $N_{H\,I} = 10^{19}$ cm^{-2} that is marked by the blue solid line. The second region, labelled 'MAX', is enclosed by the two red dashed contours where the Adams et al. (2011) model forecasts maximal SB from

gas photoionized by the UVB. The third 'SKY' region, enclosed by white dotted lines, encompasses pixels far from the region where the SB is expected to be maximal. Finally, we define two control regions ('CNT1' and 'CNT2') that will be used to test the quality of the sky subtraction and for the preparation of mock data cubes as described in the following section.

Throughout our analysis, we exclude pixels at the position of sources detected via continuum emission, a task that is easily achieved, thanks to the excellent image quality of MUSE. To this end, we run SEXTRACTOR (Bertin & Arnouts 1996) on a deep white image that we obtain by collapsing the data cube along the wavelength axis. For this, we choose the CUBEX data product, as it provides the best image quality given that the illumination correction is performed at the slice level. To ensure that the full extent of the sources are masked down to faint SB levels, we produce a segmentation map using a low detection threshold, equal to the sky root mean square (rms). To avoid the inclusion of spurious sources, the minimum area for source detection is set to 15 spaxels, corresponding to objects of $\gtrsim 0.9$ arcsec in diameter. Visual inspection confirms that the segmentation map is successful in masking all the sources where continuum emission is seen in the deep white image.

2.5 Preparation of mock data cubes

To better understand the performance of the adopted reduction techniques and to assess the presence of systematic errors throughout our analysis, we make use of mock data cubes that contain emission lines injected at wavelengths and positions chosen as described below.

All mock emission lines have Gaussian profiles with a full width at half-maximum of 2.6 Å that matches the resolving power of MUSE at the wavelength of interest, $R \sim 2550$ at $\lambda \sim 6574$ Å. As discussed below, this is the wavelength at which Hα recombination is expected given the radial velocity of UGC 7321. Mock lines are generated at three different wavelengths (see Fig. 4 for examples of observed spectra) chosen in the following way. First, we create a line with SB[5] $\mu = 2 \times 10^{-19}$ erg s^{-1} cm^{-2} arcsec^{-2} at $\lambda = 6574$ Å. This choice allows us to test whether emission at this wavelength can be recovered correctly in our analysis. This signal is injected in pixels within the CNT1 region, at a location where no signal is expected. Next, we create a line with $\mu = 2 \times 10^{-19}$ erg s^{-1} cm^{-2} arcsec^{-2} at $\lambda = 6550$ Å, which is adjacent to a bright sky line at $\lambda = 6553$ Å. This mock line is injected in both the CNT1 and CNT2 regions, and it enables tests for the presence of any bias when measuring signal in the wings of bright sky lines. Finally, we create a line with $\mu = 3 \times 10^{-19}$ erg s^{-1} cm^{-2} arcsec^{-2} at $\lambda = 6590$ Å, a wavelength free from bright sky lines. This line is injected in both the CNT1 and CNT2 regions, and it is used as a baseline calibration to test whether our procedures are flux conserving.

These mock lines are injected within individual exposures by adding flux to the data cubes that have been resampled on the final ESO data cube after performing basic calibrations only. These individual exposures are then processed as described in Sections 2.2 and 2.3 using both the CUBEX and ZAP pipelines.

---

[5] Throughout this work, we will make use of the symbol μ to identify the line SB and μ_{20} to identify the line SB in units of 10^{-20} erg s^{-1} cm^{-2} arcsec^{-2}. Similarly, we will indicate the continuum SB with the symbol μ_c and use $\mu_{20,c}$ for values in units of 10^{-20} erg s^{-1} cm^{-2} Å^{-1} arcsec^{-2}.
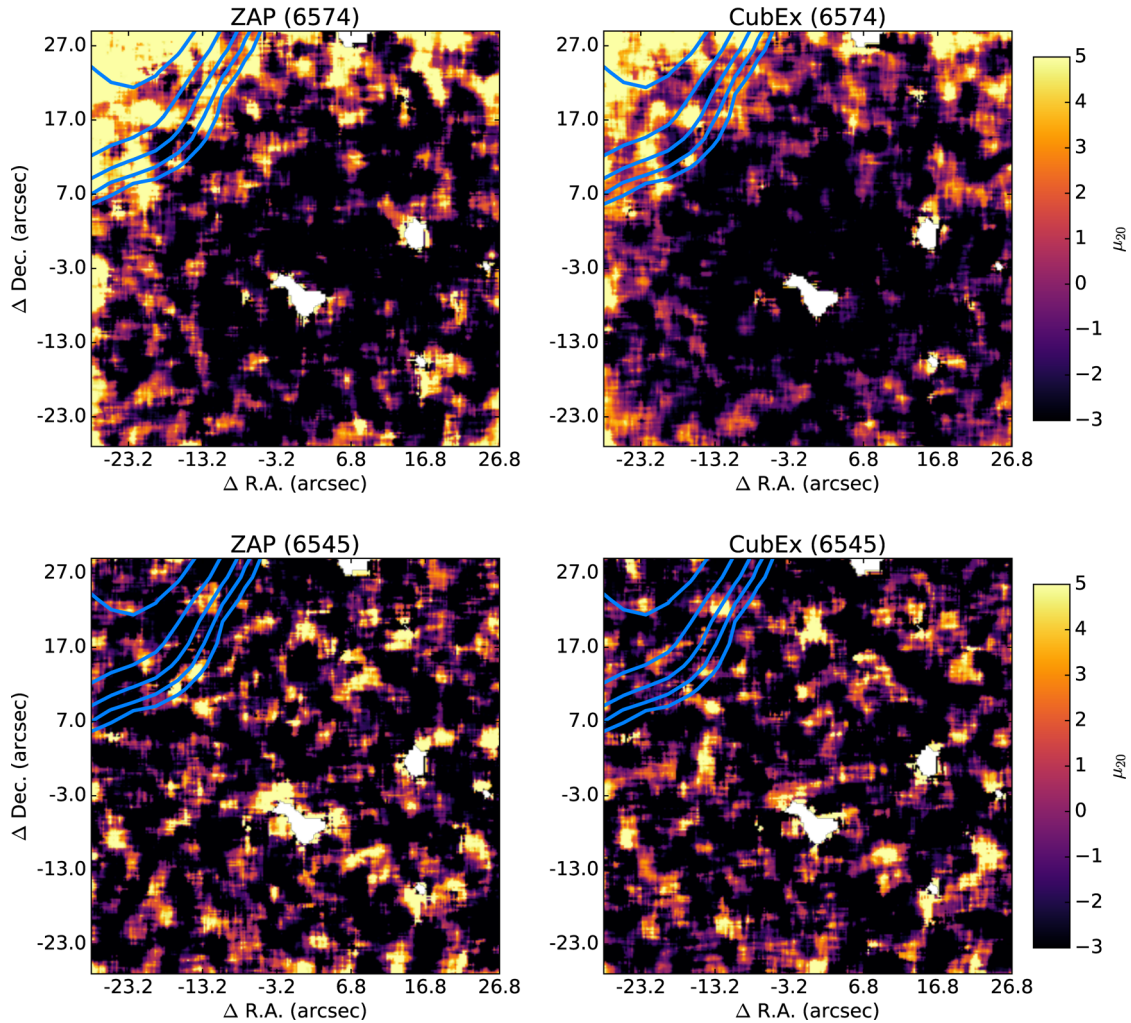
Figure 3. Optimally weighted SB maps extracted at the wavelength of the expected signal ($\lambda = 6574$ Å, top), and in a control region (bottom) centred at $\lambda = 6545$ Å, which is next to a bright sky line at $\lambda \sim 6553$ Å. North is up and east is to the left. The left- and right-hand panels show maps from the ZAP and CUBEX data cube, respectively. Data have been smoothed by a median filter with size of 1.2 arcsec. H I contours are overlaid in blue, and white patches are sources that have been masked. Extended Hα emission overlapping with the H I column density $N_{\rm H\,I} \geq 10^{19}$ cm^{-2} is visible at $\lambda \sim 6574$ Å in both the CUBEX and ZAP cubes. The lack of emission in the control regions rules out a spurious origin for this signal due to artefacts such as scattered light.

3 ANALYSIS OF MUSE OBSERVATIONS

3.1 Theoretical expectations for Hα emission near UGC 7321

The wavelength at which Hα recombination due to the ionizing UVB is expected can be computed, given the heliocentric radial velocity of UGC 7321, $v_{\rm H\,I} = 406.8 \pm 0.1$ km s^{-1} (Uson & Matthews 2003), and the galaxy rotation curve known from 21 cm observations. At the position of our observations, $v_{\rm H\alpha} \sim 510$ km s^{-1} (or $\lambda_{\rm H\alpha} = 6574$ Å) with an uncertainty of 0.5 Å (Uson & Matthews 2003; Adams et al. 2011). The emission line is expected to be unresolved at the moderate resolution of MUSE ($R \sim 2550$ at these wavelengths), but as in Adams et al. (2011), we assume a conservative window of ± 100 km s^{-1} (± 2.2 Å) over which the line can be detected due to variations in the gas velocity field across the MUSE FOV. Under the general assumption that the gas is in photoionization equilibrium, the emission line is further expected to have an order of magnitude SB of $\mu_{20} \sim 10$, with the exact normalization depending on the UVB photoionization rate and spatial location, as described in Section 4. According to the model by Adams et al. (2011), the emission is further expected to be maximal

within the region labelled H I in Fig. 2. However, we will present new models that supersede this prediction in Section 4.

3.2 Searching for Hα recombination in MUSE data

3.2.1 Analysis of two-dimensional maps

To visually evaluate if any signal is detected in MUSE data at the expected position, we extract SB maps from the ZAP and CUBEX data products by slicing the cubes in a window centred at $\lambda_{\rm H\alpha} = 6574$ Å (the top panels of Fig. 3). To maximize the signal to noise (S/N) of these maps, we compute the mean SB by summing flux along the wavelength direction while weighting according to a normalized Gaussian of width $\sigma = 1.095$ Å, which is matched to the MUSE resolution at these wavelengths. As discussed below, this procedure does not provide the best estimate for the total line flux, but it is suitable for a visual exploration of the presence of signal within maps of maximal S/N.

After applying a two-dimensional (2D) median filter of width 1.2 arcsec, visual inspection of these maps reveals the presence of
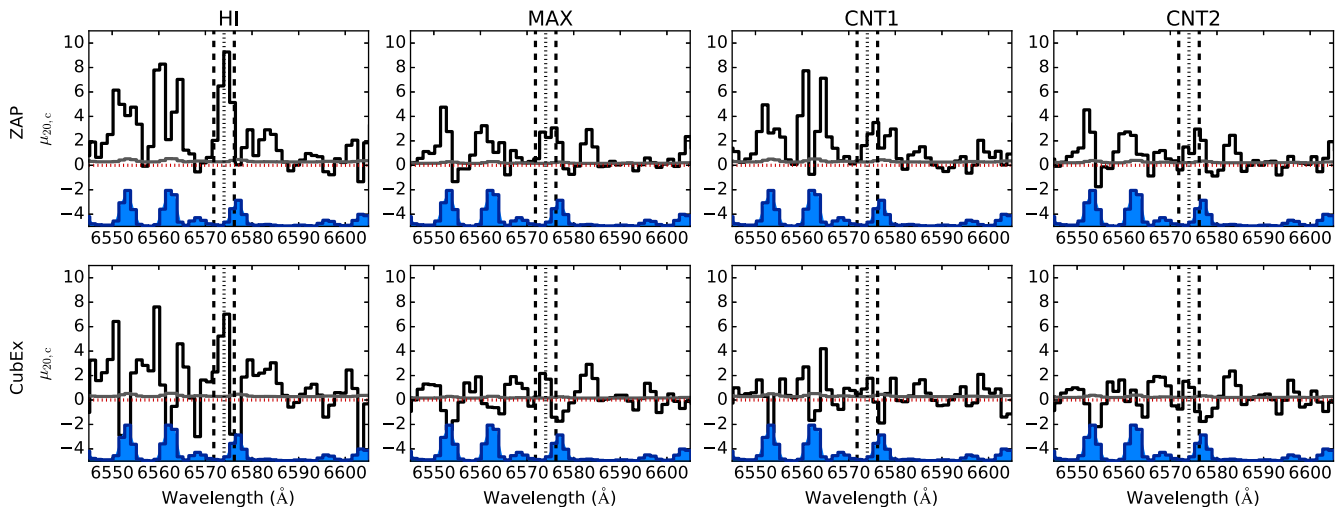
Figure 4. Gallery of mean spectra (black lines) obtained combining pixels inside the regions defined in Fig. 2, as labelled at the top of each panel. The associated statistical errors are shown in grey, and the red dotted lines mark the zero flux level. The blue filled spectra at the bottom of each panel show the mean sky SB computed from the same data. For visualization purposes, the sky flux has been scaled by a factor of 1/600 and offset to $\mu_{20} = -5$. The top row shows results from the ZAP reduction, while the bottom row shows spectra from the CUBEX reduction. The wavelength window within which the Hα emission line is expected is marked by vertical dashed lines, while the vertical dotted lines mark the expected position for the centroid of the emission line. A signal consistent with the expected Hα recombination line from UGC 7321 is detected inside the H I region in both the ZAP and CUBEX reductions.

extended emission in the north-east (top-left) corner of the FOV in both data cubes, inside the region overlapping with the 21 cm detection. Conversely, no extended emission is found in the top-right part of the FOV, within the region where the SB is expected to be maximal in the model by Adams et al. (2011), perhaps with the exception of the edge of the map. Furthermore, the presence of positive fluctuation at the outskirts of the map can be noted in the south-east direction, indicating that artefacts may be present at the edge of the FOV.

Relying again on visual inspection, we test whether the signal visible in these maps can be attributed to scattered light in one of the MUSE corners. Having produced the final data cubes by averaging exposures at different position angles, there should be no preferential direction in the final combined cubes and, in principle, any residual illumination pattern should not appear in a single corner. Nevertheless, we explicitly check for the presence of spurious scattered light as well as astrophysical signal with a broad-band spectrum by extracting SB maps centred at $\lambda = 6545$ Å, that is only $\sim$30 Å from the region where we expect the Hα emission line. Inspection of these maps (the bottom panels of Fig. 3) does not reveal a prominent positive flux, thus excluding 'white' light as the origin of the positive signal at $\lambda = 6574$ Å. Similarly, no flux excess is visible in maps extracted in a window centred at $\lambda = 6590$ Å (not shown), ruling out spurious signals with a broad spectrum.

3.2.2 Analysis of the mean spectra

Having established that data reveal a positive flux that is not associated with signal (astrophysical or instrumental) across a broad wavelength interval (with $\Delta\lambda > 40$ Å), we next characterize the spectral properties of the MUSE cubes by constructing mean spectra by averaging flux from all of the pixels inside the regions defined in Section 2.4. During this step, we exclude pixels that overlap with the position of continuum-detected sources. We also characterize the error on the mean by propagating the variance computed during data reduction, and also by means of empirical measurements of the rms in each wavelength layer. The two methods are found

to yield comparable error estimates. Finally, we ensure that flux in the regions free from sky lines in the wavelength interval $\lambda = 6483$–6493 Å and $\lambda = 6609$–6623 Å averages to zero, by subtracting a constant of $\lesssim 2 \times 10^{-20}$ erg s^{-1} cm^{-2} Å^{-1} arcsec^{-2} for the ZAP reduction and of $\lesssim 0.5 \times 10^{-20}$ erg s^{-1} cm^{-2} Å^{-1} arcsec^{-2} for the CUBEX reduction. A gallery of the mean spectra constructed for the ZAP and CUBEX cubes inside different apertures is in Fig. 4.

Additional properties of the signal seen in Fig. 3 can be inferred by inspecting the mean spectra from different apertures. First of all, in agreement with the results derived from the optimally extracted 2D maps, an emission line is detected at $\lambda \sim 6574$ Å within the H I region (left-hand panels). The significance of this detection exceeds $\sim$10σ based on statistical errors, here defined as the photon and detector noise that are estimated by propagating the variances of these contributions through the calibration and reduction procedures. However, the systematic errors are the dominant source of uncertainty, which arises from imperfect calibrations and sky residuals that are not fully corrected by the above procedures. As described below, we characterize these additional errors by means of mock data and by comparing measurements using different reduction techniques and different subsets of the data.

Fig. 4 reveals that the emission line is detected at the wavelength where Hα recombination from UGC 7321 is expected, it is visible in both the ZAP and CUBEX cubes, and it appears in the region enclosed by the H I contour with $N_{\rm HI} = 10^{19}$ cm^{-2}. Combined, these three pieces of evidence suggest that the signal seen in Figs 3 and 4 is real and that it is consistent with Hα emission from the outskirts of UGC 7321, as expected for gas photoionized by the UVB. Finally, no prominent emission is visible inside the CNT1 and the CNT2 regions (third and fourth panels in Fig. 4), indicating that the positive flux fluctuations that are visible at the west and north edge of the FOV in Fig. 3 are not related to artefacts that can mimic an emission line at the wavelength expected for Hα recombination in UGC 7321.

Moreover, no prominent signal is detected when inspecting the mean spectra in the MAX region (the second panels from the left), in agreement with what was found in the SB maps. The lack of strong signal inside the region that was predicted to contain the

strongest emission in the model by Adams et al. (2011) may appear puzzling at first. However, as we discuss in detail in Section 4, this is fully consistent with our revised photoionization model for UGC 7321. This discrepancy can be explained by the fact that the model by Adams et al. (2011) overestimated the extent of the H I profile, predicting a more extended SB profile than is warranted by current data. This unfortunate mismatch between the model by Adams et al. (2011) and the data has led us to focus our MUSE observations within a region of lower SB, with the brighter emission being confined in the corner of the FOV, in a region that overlaps with the H I emission detected at 21 cm.

Focusing again on the feature at $\lambda \sim 6574$ Å, it is evident from the spectra shown in Fig. 4 that random errors are negligible compared to the systematic uncertainty arising from residuals of bright sky lines. Indeed, the wavelength of the expected signal at $\lambda_{H\alpha} = 6574$ Å falls at just ~ 3 Å blueward of the $\lambda \sim 6577$ Å sky line, causing a partial blend at the resolution of MUSE. Furthermore, comparisons of the mean spectra in different panels reveal that the quality of the sky subtraction is lower in the north-east corner of the FOV (left-hand panels) compared to what can be achieved in the central parts of the detector (MAX and control regions, right-hand panels). We speculate that this effect is due to small errors in the geometric distortion correction and wavelength calibrations at the very edge of the FOV.

3.2.3 Additional tests on the origin of the detected signal

Given the presence of prominent residuals next to sky lines, we should take particular care when interpreting the origin of this signal and, most importantly, when quoting the significance of our measurement. To corroborate our earlier conclusion that the line detected is Hα from UGC 7321, we perform three additional tests.

First, we compare the shape of the $\lambda \sim 6574$ Å line with the shape of the residuals associated with the subtraction of the bright sky lines at $\lambda \sim 6553$ Å and $\lambda \sim 6562$ Å (Fig. 4). Residuals in the ZAP reduction, albeit strong, appear to span the entire width of these sky lines. Conversely, the line at $\lambda \sim 6574$ Å is offset from, and does not overlap with, the wavelength position of the sky residual associated with the $\lambda \sim 6577$ Å sky line. A similar behaviour is visible in the CUBEX reduction, with positive and negative residuals aligned with the sky lines at $\lambda \sim 6553$ Å and $\lambda \sim 6562$ Å, and a clearly asymmetric profile next to the $\lambda \sim 6577$ Å sky line. Furthermore, it should be noted that the emission line at $\lambda \sim 6574$ Å is the strongest feature in these spectra, despite the sky line at $\lambda \sim 6577$ Å being the faintest in this wavelength interval.

As a second test to corroborate the detection of a line at $\lambda \sim 6574$ Å, we analyse independent subsets of exposures as shown in Fig. 5. To this end, we generate mean spectra in the H I region after reconstructing two independent data cubes, using half of the total number of exposures. To simultaneously test for subtle systematic errors associated with the instrument rotation, we group exposures according to the instrument position angle. In Fig. 5, we group the 90° and 270° rotation in what we label the '90 set', and the 0° and 180° rotation in what we label the '0 set'. The resulting spectra reveal that, while the shape of the residuals associated with the $\lambda \sim 6553$ Å and $\lambda \sim 6562$ Å sky lines change with the instrument position angle in both the CUBEX and ZAP reductions, the line at $\lambda \sim 6574$ Å is consistently recovered with a similar shape, as expected for an astrophysical signal.

As a third and final test, we make use of the mock cubes described in Section 2.5. Using mock data, we check explicitly whether the shape of the sky residuals discussed above is a trustworthy indicator
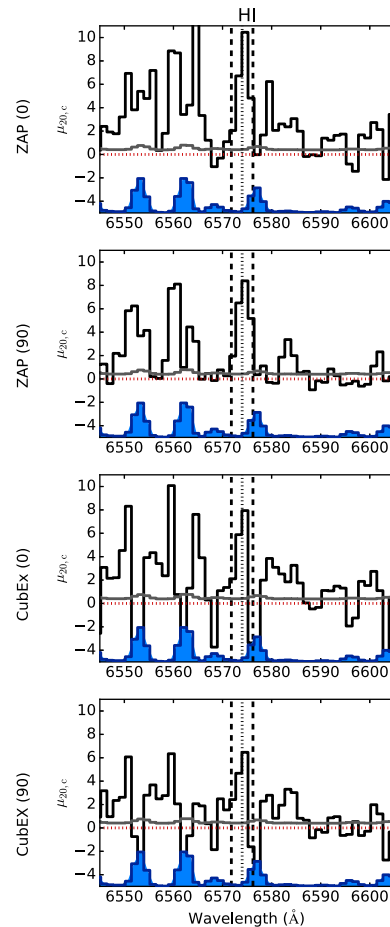

Figure 5. Same as Fig. 4, but for the mean spectra extracted in the H I region using independent subsets of exposures obtained at position angles of 0°/180° (labelled 0) and 90°/270° (labelled 90). Spectra from ZAP cubes are shown in the top two panels, while spectra from CUBEX cubes are shown in the bottom two panels. A line at $\lambda \sim 6574$ Å is consistently detected in independent sets of exposures.

of the presence of a line at $\lambda \sim 6574$ Å. For this, we inject mock lines with the spectral properties shown in the bottom panels of Fig. 6 and we perform illumination corrections and sky subtraction using the same pipelines used for the data. Particularly relevant for our test is the fact that the mock line at $\lambda \sim 6550$ Å is offset by ~ 3 Å from a sky line, as is the case for the line at $\lambda \sim 6574$ Å compared to the $\lambda \sim 6577$ Å sky line. Focusing on the H I region first (left-hand panels of Fig. 6), it is evident that the mock line at $\lambda \sim 6550$ Å is recovered by our analysis. The spectra also exhibit a residual with a prominent excess at bluer wavelengths, similar to the feature at $\lambda \sim 6574$ Å where the astrophysical signal is expected and no mock line is injected.

The right-hand panels of Fig. 6 show how mock emission lines, including the mock signal at $\lambda \sim 6574$ Å, are recovered inside the CNT2 region in both the ZAP and CUBEX reductions. This implies that our reduction procedures are flux conserving and that the lack of appreciable emission in the MAX region (Fig. 4) is genuine and not attributable to improper sky subtraction. Most notably, the mock line at $\lambda \sim 6590$ Å that is far from sky lines is recovered with very high precision and accuracy, implying that MUSE is potentially well suited for measurements with $\lesssim 10$ per cent error. We will return to this point in Section 5.
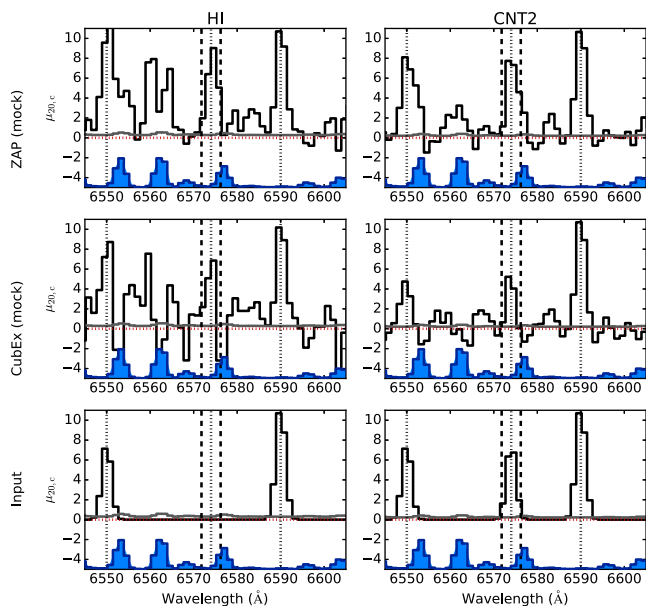
Figure 6. Same as Fig. 4, but for mean spectra obtained after injecting mock lines as described in Section 2.5, the position of which is marked by vertical dotted lines. The input mock spectra are shown in the bottom panels, while the top and middle panels show the recovered SB for the ZAP and CUBEX reductions, respectively. Despite noticeable contamination arising from the wings of sky lines, the mock emission lines are recovered at the expected locations.

In summary, we have shown that (i) a feature is detected at $\lambda \sim 6574$ Å and it is consistently present in two independent data reductions and in two independent sets of exposures with different instrument rotations; (ii) the recovered line has a profile consistent with real signal close to a sky line and (iii) the emission overlaps with the location where H I is detected with $N_{\mathrm{H\,I}} \gtrsim 10^{19}$ cm^{-2}. Altogether, these pieces of evidence corroborate the detection of an extended low SB signal that is consistent with our expectation of Hα emission from gas that recombines following photoionization from the UVB at the edge of UGC 7321.

3.3 Measurement of the detected emission line

In the previous section, we have shown how data support the detection of Hα emission in the outskirts of UGC 7321. However, our analysis has also demonstrated that strong residuals associated with sky lines are present and that they dominate the error budget in our measurement. In this section, we attempt to quantify the amplitude of this systematic uncertainty.

Starting with the analysis of the 1D spectra shown in Fig. 4, we integrate the SB within a ± 2.2 Å window (as justified in Section 3.1) around the wavelength $\lambda_{\mathrm{H\alpha}} = 6574$ Å, finding $(1.4 \pm 0.1) \times 10^{-19}$ erg s^{-1} cm^{-2} arcsec^{-2} for the CUBEX reduction and $(2.6 \pm 0.1) \times 10^{-19}$ erg s^{-1} cm^{-2} arcsec^{-2} for the ZAP reduction. Here, the uncertainty quoted for individual measurements reflects only the statistical error. The reason for the different SB values is attributable to the fact that the CUBEX reduction appears to better suppress the sky line residuals when compared with the ZAP reduction. This effect can be quantified using mock data. Indeed, for an input mock line of 2×10^{-19} erg s^{-1} cm^{-2} arcsec^{-2} at $\lambda = 6550$ Å, we recover an integrated signal of $(2.2 \pm 0.1) \times 10^{-19}$ erg s^{-1} cm^{-2} arcsec^{-2} from the CUBEX reduction. Conversely, the ZAP reduction yields an integrated SB of $(3.5 \pm 0.1) \times 10^{-19}$

erg s^{-1} cm^{-2} arcsec^{-2}, revealing that positive residuals of the order of $\sim 1 \times 10^{-19}$ erg s^{-1} cm^{-2} arcsec^{-2} are present next to sky lines. Far from the wings of the sky lines (e.g. at $\lambda \sim 6590$ Å), both reduction techniques are able to recover the input line SB to within the associated statistical errors of ~ 5 per cent. Based on this analysis, in the following we assume that the CUBEX reduction yields a more accurate value for the line SB.

To estimate the amplitude of the systematic uncertainty, we proceed as follows. First, we measure the SB values for the two independent cubes that we obtain by combining independent sets of data, finding consistent values of $(1.5 \pm 0.1) \times 10^{-19}$ erg s^{-1} cm^{-2} arcsec^{-2} and $(1.4 \pm 0.1) \times 10^{-19}$ erg s^{-1} cm^{-2} arcsec^{-2} for the 0 and 90 sets, respectively. This finding rules out the presence of systematic differences associated with the instrument rotation. However, by integrating the line SB within the control regions defined above both at $\lambda = 6550$ Å and at $\lambda = 6574$ Å, we find fluctuations that are up to one order of magnitude higher than the quoted variance based on statistical uncertainties. By comparing measurements in these control apertures, we find a dispersion of $\sim 5 \times 10^{-20}$ erg s^{-1} cm^{-2} arcsec^{-2}, which we consider a more realistic estimate of the uncertainty of our measurement.

Finally, we perform two additional tests. First, we perform the wavelength integral on the CUBEX reduction by first collapsing the cube along the wavelength direction and then adding the SB in pixels within the regions defined in Fig. 2. In this case, we find a line SB of $(1.1 \pm 0.1) \times 10^{-19}$ erg s^{-1} cm^{-2} arcsec^{-2}, again with a scatter of ~ 3–4×10^{-20} erg s^{-1} cm^{-2} arcsec^{-2} within the control apertures. Also in this case, the analysis of the two independent rotations yields consistent results. Next, we perform the integration by considering a larger wavelength window of $\lambda = 6569$–6581 Å, chosen to encompass the sky line at $\lambda \sim 6577$ Å. This choice is dictated by the fact that, by construction, the CUBEX reduction is flux conserving across wavelength windows that are larger than the widths of the sky lines. In agreement with the previous measurements, we find a value of $(1.1 \pm 0.1) \times 10^{-19}$ erg s^{-1} cm^{-2} arcsec^{-2}.

In summary, by analysing both the 1D spectra and the 2D line maps at the position expected for Hα recombination due to the ionization from the UVB in our updated models for UGC 7321 (see Section 4), we find consistent indications of the presence of a line with SB $(1.2 \pm 0.1 \pm 0.5) \times 10^{-19}$ erg s^{-1} cm^{-2} arcsec^{-2}. Here, the first error indicates the statistical uncertainty and the second error characterizes the presence of an additional systematic uncertainty in proximity to the bright sky line at $\lambda \sim 6577$ Å and at the edges of the FOV. This value is fully consistent with the detection reported by Uson et al.[6] of $(0.96 \pm 0.14) \times 10^{-19}$ erg s^{-1} cm^{-2} arcsec^{-2}.

4 CONSTRAINTS ON THE UVB INTENSITY

After presenting an overview of our new radiative transfer calculations in Section 4.1, in Section 4.2 we describe the procedure adopted to constrain the H I photoionization rate ($\Gamma_{\mathrm{H\,I}}$) starting from the observed Hα SB.

4.1 Photoionization modelling of UGC 7321

To predict the Hα SB as a function of the UVB intensity, we construct a photoionization model for UGC 7321, improving upon the analytic calculations presented in Adams et al. (2011).

---

[6] See http://iactalks.iac.es/talks/view/393.

4.1.1 Description of the photoionization code

We model the hydrogen density of UGC 7321 as an exponential disc

$$n_\mathrm{H}(R, \bar{z}) = n_{\mathrm{H},0} \exp\left(-R/h_\mathrm{R}\right) \exp\left(-|\bar{z}|/h_\mathrm{z}\right), \qquad (1)$$

where $n_\mathrm{H}(R, \bar{z})$ is the total hydrogen number density in cylindrical coordinates $(R, \bar{z})$, $n_{\mathrm{H},0}$ defines the central density, while h_R and h_z are, respectively, the radial scalelength and vertical scaleheight of the disc. For a given external and isotropic UVB, we solve for the vertical ionization and temperature of the disc at a fixed radial distance R assuming a two-sided plane parallel geometry. In this way, we are effectively reducing the full three-dimensional radiative transfer problem to a series of 1D calculations. The full structure of the galaxy in terms of temperature and ionization fraction is thus reconstructed combining results of calculations with plane-parallel geometries at different R. Such approximation is expected to give results that are accurate to within 20–30 per cent when compared with a full three-dimensional calculation (see e.g. Dove & Shull 1994).

Details of the adopted radiative transfer scheme are described in Haardt & Madau (2012). Briefly, the ionization and thermal vertical structure is solved iteratively for an input power-law spectrum with spectral slope 1.8. Ionization equilibrium is achieved by balancing radiative recombinations with photoionization, including the formation and propagation of recombination radiation from H II, He II and He III. For the thermal structure, photoheating is balanced by free–free, collisional ionization and excitation, and recombinations from H II, He II and He III. In our calculation, we assume a number density ratio He/H = 1/12. A current limitation of the model is that we do not include metal lines nor dust.

Once the ionization and thermal state of the gas are known, we compute the Hα emissivity as

$$\epsilon_{\mathrm{H}\alpha}(R, \bar{z}) = h\nu_{\mathrm{H}\alpha}\alpha_{\mathrm{H}\alpha}^{\mathrm{eff}}(T)\, n_\mathrm{p}(R, \bar{z})n_\mathrm{e}(R, \bar{z}), \qquad (2)$$

where n_p and n_e are the proton and electron number densities, and $\alpha_{\mathrm{H}\alpha}^{\mathrm{eff}}$ is the effective case A recombination rate taken from Pequignot, Petitjean & Boisson (1991). Finally, we derive the H I column density and the Hα SB maps from an integration along the line of sight of the neutral hydrogen number density and Hα emissivity. Specifically, for a given viewing angle i, we compute the projected maps of $N_{\mathrm{H\,I}}(b_1, b_2)$ and $\mu(b_1, b_2)$, where b_1 and b_2 describe a new coordinate system along the semimajor and semiminor axis of the projected ellipse. The relations connecting the cylindrical coordinate system $(R, \bar{z})$ to the projected position (b_1, b_2) can be easily obtained from the following coordinate transformations (e.g. Adams et al. 2011):

$$|\bar{z}| = |\rho \cos i + b_2 \sin i| \qquad (3)$$

and

$$R = \sqrt{(\rho \sin i - b_2 \cos i)^2 + b_1^2}. \qquad (4)$$

Here, ρ, which ranges from $-\infty$ to $+\infty$, is the distance from the projected disc mid-plane along the line of sight.

4.1.2 Model predictions and general considerations

Before turning our attention to the modelling of UGC 7321, we present results from our radiative transfer calculations to highlight how observations of the H I column density combined with observations of the Hα SB can constrain the H I photoionization rate.

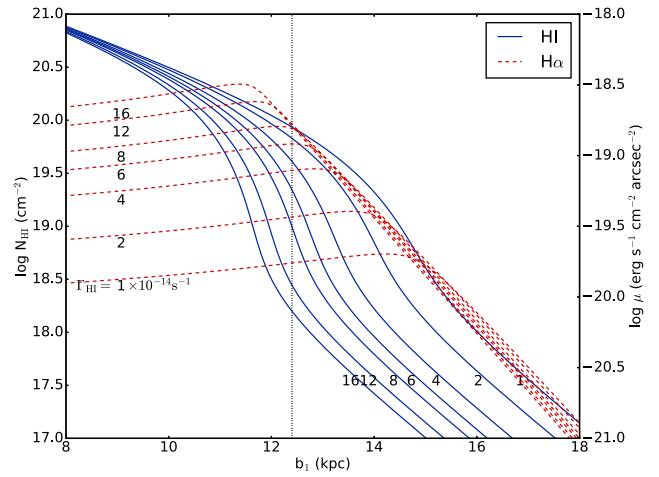**Figure 7.** H I profiles (blue solid lines, left-hand side axis) and Hα SB profiles (red dashed lines, right-hand side axis) extracted along the mid-plane ($b_2 = 0$) of a disc with constant parameters ($n_{\mathrm{H},0} = 1.5\,\mathrm{cm}^{-3}$, $h_\mathrm{R} = 2300\,\mathrm{pc}$, $h_\mathrm{z} = 426\,\mathrm{pc}$) observed at an inclination of $i = 84°$. Different curves are for different radiative transfer calculations with varying intensity of the UVB, as labelled by the respective values for $\Gamma_{\mathrm{H\,I}}$ in units of $10^{-14}\,\mathrm{s}^{-1}$. The position of the $N_{\mathrm{H\,I}} = 10^{19}\,\mathrm{cm}^{-2}$ contour for UGC 7321 is marked by the dotted black line. For a fixed density distribution, higher values of $\Gamma_{\mathrm{H\,I}}$ shift the ionization front to smaller b_1. The location of the maximum SB tracks the hydrogen ionization front. The SB becomes nearly independent of b_1 at small radii, with an amplitude that is proportional to $\Gamma_{\mathrm{H\,I}}$.

In Fig. 7, we show the H I column density and the corresponding Hα SB profiles computed along the mid-plane of a projected disc ($b_2 = 0$), which is defined by $n_{\mathrm{H},0} = 1.5\,\mathrm{cm}^{-3}$, $h_\mathrm{R} = 2300\,\mathrm{pc}$ and $h_\mathrm{z} = 426\,\mathrm{pc}$. The disc is observed at an inclination of $i = 84°$, which is consistent with the inclination of UGC 7321 (Adams et al. 2011), and the different profiles are for different values of the H I photoionization rate, $\Gamma_{\mathrm{H\,I}} = (1, 2, 4, 6, 8, 12, 16) \times 10^{-14}\,\mathrm{s}^{-1}$. Trends that are common for this type of calculations can be found in this figure (e.g. Dove & Shull 1994; Adams et al. 2011). Focusing on the H I column-density profiles, it is evident that the location of the ionization front – where hydrogen turns from highly ionized ($N_{\mathrm{H\,I}} \leq 10^{17}\,\mathrm{cm}^{-2}$) to fully neutral ($N_{\mathrm{H\,I}} \geq 10^{20}\,\mathrm{cm}^{-2}$) – moves to smaller radii with increasing H I photoionization rate. The associated Hα SB profile behaves similarly. The SB is maximal at the location of the ionization front, and drops off rapidly towards larger radii and slowly towards smaller radii. Gas to the left of the ionization front is neutral along the mid-plane (for $\bar{z} = 0$), and Hα emission arises from a skin of ionized gas above and below the mid-plane that is observed in projection at $b_2 = 0$.

Given that the shape of the H I profiles varies with $\Gamma_{\mathrm{H\,I}}$, observations of the location of this ionization front in H I maps can be used to constrain the intensity of the UVB (see also e.g. Dove & Shull 1994). However, this measurement is clearly degenerate with the structural parameters that define the gas density distribution. This degeneracy is highlighted in Fig. 8, which shows the H I and Hα profiles from a grid of models at constant $\Gamma_{\mathrm{H\,I}} = 8 \times 10^{-14}\,\mathrm{s}^{-1}$, but with different parameters describing the structure of the disc. Starting with a fiducial model defined by $n_{\mathrm{H},0} = 1.5\,\mathrm{cm}^{-3}$, $h_\mathrm{R} = 2300\,\mathrm{pc}$, $h_\mathrm{z} = 426\,\mathrm{pc}$ (ID 712), we construct a grid varying each parameter one at the time, as shown in Fig. 9. All models are observed at an inclination angle of 84°. Comparing Figs 7 and 8, it is clear that the location of the ionization front is a sensitive function of the parameters describing the density distribution of the disc, making accurate determinations of the UVB intensity from H I data alone very difficult.
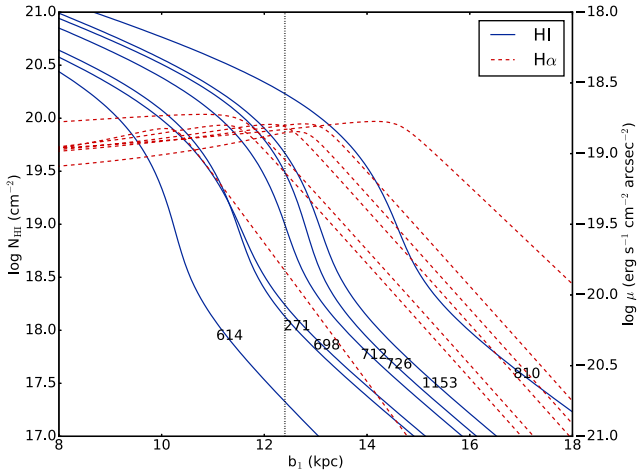
Figure 8. Same as Fig. 7, but for discs with different structural parameters (discussed in the text, curves are labelled with the identifier of the model as in Fig. 9), which are illuminated by a constant UVB with $\Gamma_{\mathrm{H}\,\textsc{i}} = 8 \times 10^{-14}\,\mathrm{s}^{-1}$. Any inference on the properties of the UVB from H\,\textsc{i} maps alone suffers from a degeneracy between the gas density profile and its ionization state. However, the Hα SB is only weakly dependent on the density distribution for radii interior to the ionization front.

And while the H\,\textsc{i} profiles in predominantly neutral regions can be used to constrain the choice of structural parameters for a given galaxy, co-variance among these parameters and/or local deviations of the density profile from a single exponential may lead to incorrect extrapolations at larger radii, resulting in significant errors on the inferred photoionization rate when using 21 cm data only.

However, Fig. 8 shows that the value of the Hα SB interior to the ionization front is only weakly dependent on the disc's parameters, in spite of the large scatter in the location of the ionization front itself or in the shape of the H\,\textsc{i} profile. Thus, while H\,\textsc{i} data alone provide only weak constraints on the photoionization rate, a joint analysis of the radial H\,\textsc{i} column density and the Hα SB profile has the potential of pinning down $\Gamma_{\mathrm{H}\,\textsc{i}}$ to better than a factor of 2 for fiducial values of $\Gamma_{\mathrm{H}\,\textsc{i}} \sim (6-8) \times 10^{-14}\,\mathrm{s}^{-1}$ (see below). Moreover, by exploiting MUSE's capability of obtaining spatially resolved maps of the Hα SB, one can derive even tighter constraints on the photoionization rate through a joint analysis of the H\,\textsc{i} and Hα maps in two dimensions. We do not attempt such a detailed analysis here, given the large uncertainty in the current line flux measurements. Thus, in the following, we simply offer a qualitative description of the advantages of resolving the spatial distribution of the Hα SB.

In Fig. 9, we present the 2D maps for the same models shown in Fig. 8. This gallery visually confirms how models illuminated by a constant UVB with $\Gamma_{\mathrm{H}\,\textsc{i}} = 8 \times 10^{-14}\,\mathrm{s}^{-1}$ consistently reach a mean SB of $\sim 8 \times 10^{-20}\,\mathrm{erg\,s}^{-1}\,\mathrm{cm}^{-2}\,\mathrm{arcsec}^{-2}$ interior to the ionization front. However, differences in the underlying density distribution
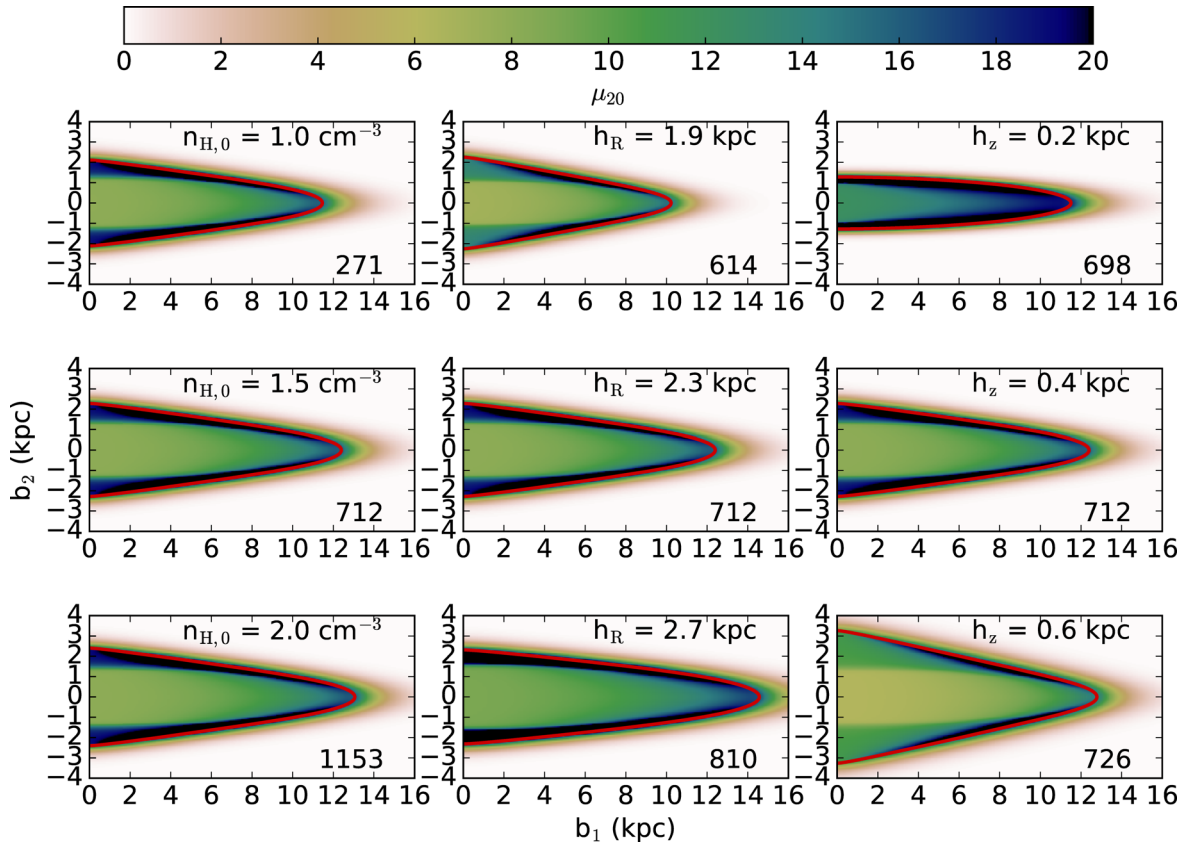
Figure 9. Gallery of Hα SB maps of a disc viewed at an inclination of $i = 84°$ and illuminated by UVB with $\Gamma_{\mathrm{H}\,\textsc{i}} = 8 \times 10^{-14}\,\mathrm{s}^{-1}$. Starting from a fiducial model with $n_{\mathrm{H},0} = 1.5\,\mathrm{cm}^{-3}$, $h_{\mathrm{R}} = 2300\,\mathrm{pc}$, $h_z = 426\,\mathrm{pc}$ (model 712, in the middle row), each column shows results of different discs obtained by varying structural parameters one at the time, as labelled in the top-right corner of each panel. The red line marks the contour at $N_{\mathrm{H}\,\textsc{i}} = 10^{19}\,\mathrm{cm}^{-2}$. Profiles extracted from these models are shown in Fig. 8, labelled by their ID number in the bottom-right corner of each panel. By combining spatially resolved maps of H\,\textsc{i} and Hα emission, one can discriminate among different models to accurately measure $\Gamma_{\mathrm{H}\,\textsc{i}}$.

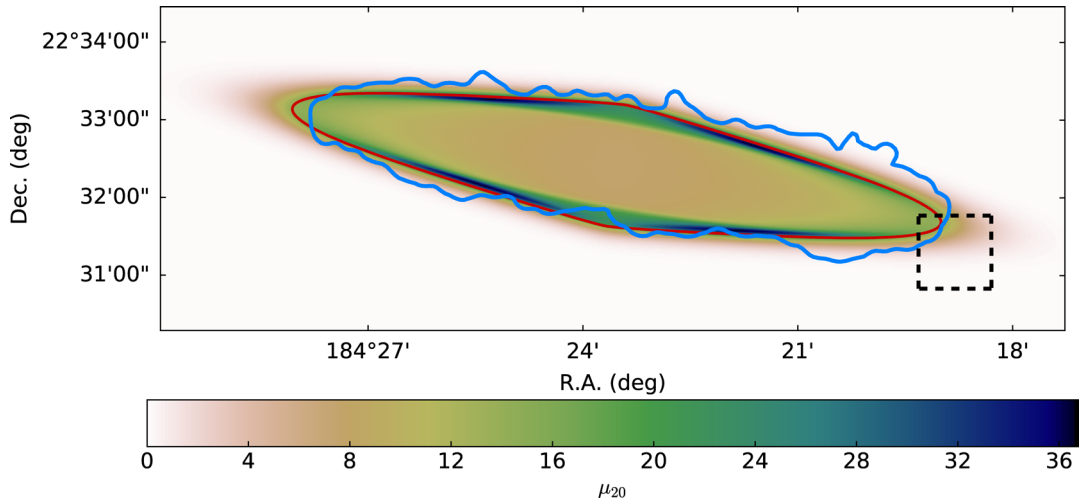**Figure 10.** Hα SB map for the model in our grid that more closely reproduces both the observed Hα SB and the size of the H I contours at $N_{H I} = 10^{19}$ cm^{-2}. The light blue line is the observed H I contour at $N_{H I} = 10^{19}$ cm^{-2}, while the red line marks the location predicted by the model. The MUSE FOV is indicated by the black dashed line. Our observations constrain the photoionization rate to be in the range $\Gamma_{H I} \sim (6-8) \times 10^{-14}$ s^{-1}. However, due to the unknown contribution from local sources of ionization, we caution that these values should be regarded as formal upper limits.

result in characteristic shapes of the 2D SB maps. In particular, the location and shape of the brightest regions, which originate from projections effects of the ionization front, are sensitive to the parameters describing the density distribution and, not shown here, to the viewing angle. It follows that precise determinations of the H I photoionization rate are possible provided that one resolves these features in Hα SB maps, which can be analysed jointly with the H I column density from 21 cm maps.

4.2 The UVB photoionization rate at $z \sim 0$

4.2.1 Constraints on $\Gamma_{H I}$

Following the procedure outlined in the previous section, we combine information from the H I column density and the Hα SB maps to translate our measurement into a value of the H I photoionization rate. We start by constructing a grid of ∼5000 radiative transfer models for exponential discs, varying the central density in the interval $n_{H,0} = 1-6$ cm^{-3} in steps of 0.5 cm^{-3}, the disc scalelength in the interval $h_R = 1.3-2.9$ kpc in steps of 200 pc and the disc scaleheight in the interval $h_z = 100-700$ pc in steps of 100 pc. These intervals are chosen to bracket the best-fitting parameters for UGC 7321, as listed in table 1 of Adams et al. (2011). Similarly, the step size is chosen to be comparable to the statistical errors on these measurements. For each combination of disc parameters, we perform the radiative transfer calculation for seven different values of the UVB intensity, $\Gamma_{H I} = (1, 2, 4, 6, 8, 12, 16) \times 10^{-14}$ s^{-1}.

Finally, H I column densities and Hα SB maps are reconstructed projecting each model along three viewing angles ($i = 82°, 83°, 84°$), with values chosen to bracket the inclination of UGC 7321 in the plane of the sky as determined by Adams et al. (2011). We note that the inclination angle of UGC 7321 is uncertain, with Matthews, Gallagher & van Driel (1999) suggesting $i = 88°$ (see also Uson & Matthews 2003). This discrepancy reflects the difficulty of measuring inclinations for edge-on discs. In this work, we prefer to adopt a lower inclination angle, which appears to better reproduce the aspect ratio of the H I disc for UGC 7321 at large radii, beyond the optical radius. We note that progressively higher inclination angles yield brighter and sharper ionization fronts, thus introducing

an uncertainty in the inferred value for $\Gamma_{H I}$ that is comparable to the error in the SB measurement. As we discussed qualitatively in the previous section, future observations that can map the extent of the ionization front will be able to reduce this additional source of uncertainty.

Next, we select models that best reproduce the available observations by imposing the following two constraints on the grid of projected H I and Hα maps. First, we demand that the semimajor and semiminor axes measured in models at $N_{H I} = 10^{19}$ cm^{-2} match the observed values of $b_{1,H I} = 12.4 \pm 0.1$ kpc and $b_{2,H I} = 2.3 \pm 0.2$ kpc within the associated errors. Secondly, we require that the Hα SB computed in models at the same location of our MUSE observations is consistent with the observed value within the associated errors. After imposing these two constraints, three models are found to provide a good fit to both the H I and the Hα observations. The best match, model ID 712, is shown in Fig. 10.

The three models that best reproduce the available observations are characterized by disc parameters in the range $n_{H,0} = 1-2$ cm^{-3}, $h_R = 2.1-2.5$ kpc and $h_z = 426$ pc. The disc scalelength and scaleheight are consistent with the best-fitting parameters inferred by Adams et al. (2011), obtained by modelling the observed H I profiles. Compared to their analysis, however, our models prefer smaller values for $n_{H,0}$ that, as shown in Fig. 9, result in a smaller radius of the ionization front.

This discrepancy arises from having imposed different constraints on the models. In their analysis, Adams et al. (2011) constrain their model to reproduce the H I profile at radii between 9 and 11 kpc, and they extrapolate the best-fitting model to larger radii. Conversely, in our analysis, we impose that the location of the $N_{H I} = 10^{19}$ cm^{-2} contour in the model is also what is observed in the 21 cm map, without requiring that models track observations in the neutral regions at small radii. The fact that these different choices yield different best-fitting models is simply because the H I disc in the observed galaxy is not a perfect exponential. Given our choice and after simultaneously computing the properties of the H I and Hα maps as a function of the H I photoionization rate, our radiative transfer calculations predict that the maximal emission in UGC 7321 should occur in a region that overlaps with the H I region (see Fig. 10), at radii further in than predicted by the model of Adams

et al. (2011). Indeed, their fig. 2 suggests that an extrapolation of the best-fitting H I profile is overestimating the radius of the H I contour at $N_{H I} = 10^{19}$ cm^{-2} and, consequently, it is overestimating the extent of the region with maximal SB. Conversely, our self-consistent calculation of the gas ionization state and emissivity shows that the lack of significant detection in the MAX region where the maximal emission was originally expected is in fact fully consistent with a model in which gas at the edge of UGC 7321 is photoionized by the UVB.

The models that more closely reproduce observations have H I photoionization rates in the range of $\Gamma_{H I} \sim (6-8) \times 10^{-14}$ s^{-1}. We emphasize that this range does not represent a formal confidence interval on $\Gamma_{H I}$, as it simply reflects the photoionization rates of models that are present in our grids and that provide a good description of our observations. A more formal estimate of the photoionization rate can be obtained, for instance, coupling the results of our radiative transfer code with Markov chain Monte Carlo methods. However, given the large uncertainty currently affecting the measured SB, we defer this approach to future work.

4.2.2 Caveats on ionization mechanisms other than the UVB

Before comparing our findings with previous work, we note that the inferred value of $\Gamma_{H I}$ should be regarded as a formal upper limit on the UVB photoionization rate. Indeed, in addition to recombination from gas photoionized by the UVB, Hα emission in proximity to a galaxy may arise from photoionization due to local sources or from ionizing photons that escape from the inner star-forming disc (e.g. Voges & Walterbos 2006; Oey et al. 2007). Furthermore, processes other than photoionization may operate at the disc–halo transition, as seen for instance within the diffuse ionized medium in nearby galaxies (e.g. Hoopes & Walterbos 2003; Calzetti et al. 2004). With current data, we cannot easily constrain the nature of the ionization mechanism, as detailed modelling would require, for instance, the detection of metal lines in deeper exposures (e.g. Bland-Hawthorn et al. 1997). We note, however, that a significant contribution from local sources is unlikely, as MUSE observations would in fact resolve H II regions with sizes of $\gtrsim 30$ pc. Even accounting for smaller unresolved H II regions at the position of our observations, we do not expect star formation on scales of $\gtrsim 10$ arcsec (or $\gtrsim 500$ pc) in the outer H I disc of UGC 7321.

To assess instead the contribution of ionizing photons from the central star-forming regions to the total ionization budget, we use the STARBURST99 code (Leitherer et al. 1999) to generate a spectral energy distribution L_ν for UGC 7321. In this calculation, we assume a star formation rate of ~ 0.6 M$_\odot$ yr^{-1} based on the observed UV flux (Karachentsev & Kaisina 2013). The maximum contribution of local sources to the photoionization rate at the position of our observations is

$$\Gamma_{H I, loc} = \int_{\nu_0}^{\infty} d\nu \frac{L_\nu}{4\pi R^2 h\nu} \sigma_{H I}(\nu) \sim 2.6 \times 10^{-11} \text{ s}^{-1}, \quad (5)$$

where the numerical value for $\sigma_{H I}$ is from Verner et al. (1996), and $R = 12.5$ kpc is the distance from the observed position to the centre of the galaxy.

This calculation (see also Schaye 2006) implies that massive stars in the disc of UGC 7321 can easily account for, and exceed, the photoionization rate inferred by our observations. However, by targeting the tip of the H I disc, we maximize the optical depth seen by ionizing photons that leak from the central stellar disc. As shown by the locations of the H I contours in Fig. 1, photons leaking along the mid-plane would see an optical depth at

$\lambda \sim 912$ Å of $\tau_{912} \gg 1000$ and, although the small-scale structure of the ISM is likely to be very different from that of a simple slab, the presence of column density in excess of $N_{H I} = 10^{21}$ cm^{-2} makes it quite unlikely that ionizing photons escape along the disc's mid-plane. The assumed geometry for the calculation of the optical depth at the mid-plane is also justified, to first order, by the fact that UGC 7321 does not exhibit a prominent central bulge and that its disc does not present notable irregularities in the stellar or H I distribution (Matthews et al. 1999; Uson & Matthews 2003).

We conclude that the Hα emission at the location of our observations is primarily driven by photoionization arising from the UVB. We think it is unlikely that other sources contribute significantly but cannot rule out that ionizing photons from the galaxy itself or from other sources contribute as well. Therefore, we can only place a formal upper limit on the H I photoionization rate of the UVB with current data, but we regard our measurement at the edge of the H I disc as a bona fide estimate of the intensity of the ionizing UVB.

4.2.3 Comparison with other work

In Fig. 11, we compare our inferred values for $\Gamma_{H I}$ with predictions from models of the UVB and with other estimates from the recent literature. Our measurement, taken at face value, is in disagreement with the 5σ upper limit on $\Gamma_{H I}$ reported by Adams et al. (2011) in the same galaxy UGC 7321, despite their SB upper limit being consistent with our detection. This discrepancy highlights how detailed radiative transfer calculations are required when converting the Hα SB into a photoionization rate. As the quality of SB measurements are likely to improve in the near future (see below), more detailed modelling is therefore warranted to characterize the systematic uncertainty that affects the conversion between observables (μ) and physical quantities ($\Gamma_{H I}$). Considering instead the photoionization rates inferred from the statistics of the low-redshift ($z \sim 0.1$) Lyα forest, our values for $\Gamma_{H I}$ are in line with the recent analyses by Shull et al. (2015), Viel et al. (2016), and Gaikwad et al. (2016). These authors consistently find values in the interval $\Gamma_{H I} \sim (5-10) \times 10^{-14}$ s^{-1} (but see Kollmeier et al. 2014), albeit relying for most part on the analysis of the same data. Extrapolated to $z \sim 0$, these studies predict $\Gamma_{H I} \sim (4-5) \times 10^{-14}$ s^{-1}, below but broadly consistent with our determination of $\Gamma_{H I} \sim (6-8) \times 10^{-14}$ s^{-1}.

Turning our attention to models of the UVB, we note that cosmological radiative transfer calculations predict photoionization rates that bracket current measurements. Indeed, both our measurement and the study of the $z \sim 0.1$ Lyα forest imply H I photoionization rates at intermediate values relative to those predicted by the Haardt & Madau (2012) and Faucher-Giguère et al. (2009) models (at the lower end) and by the Haardt & Madau (2001) model (at the upper end). Fig. 11 also suggests that, as already discussed in the literature (e.g. Kollmeier et al. 2014; Khaire & Srianand 2015; Shull et al. 2015), the recent Haardt & Madau (2012) UVB model may underestimate $\Gamma_{H I}$ by a factor of $\sim 2-3$. The new Madau & Haardt (2015) model, which has been recalculated with updated quasar emissivity (see also Khaire & Srianand 2015; Cristiani et al. 2016), lies instead in the range allowed by observations. However, the large scatter among measurements both at $z \sim 0$ (e.g compare our value and the limit by Adams et al. 2011) and at $z \sim 0.1$ (e.g. compare Kollmeier et al. 2014; Shull et al. 2015) imply that current measurements still suffer from up to a factor ~ 2 uncertainty, and better accuracy is needed to further inform and refine models.
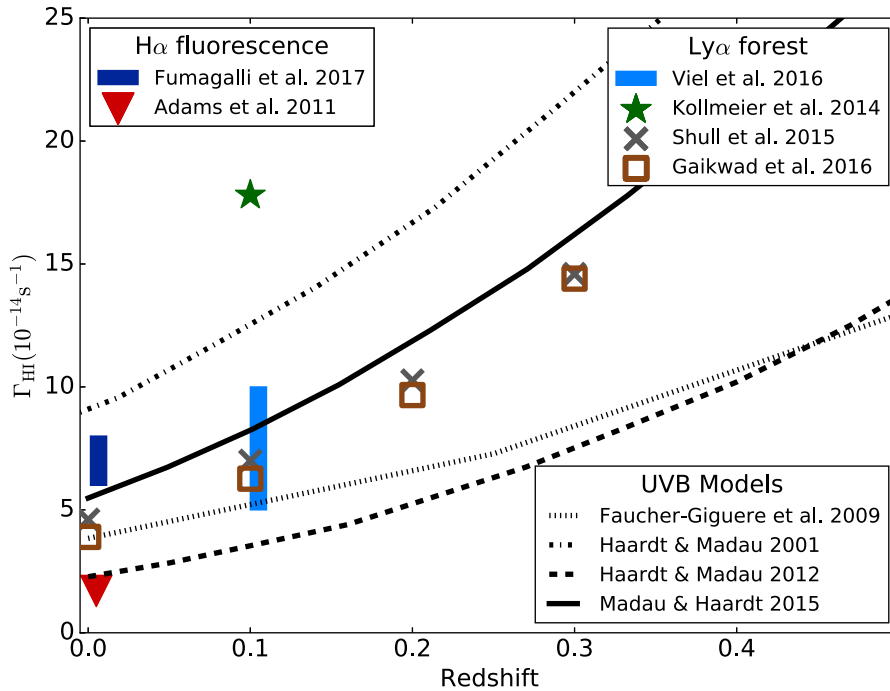
Figure 11. Summary of current models and constraints of UVB photoionization rate at $z < 0.1$. Predictions from UVB models from Haardt & Madau (2001), Faucher-Giguère et al. (2009), Haardt & Madau (2012) and Madau & Haardt (2015) are displayed with lines. Values inferred from statistics of the Lyα forest from Kollmeier et al. (2014), Shull et al. (2015), Viel et al. (2016) and Gaikwad et al. (2016) are shown with symbols. The upper limit inferred by Adams et al. (2011) is also shown in comparison with our measurement.

5 SUMMARY AND FUTURE PROSPECTS

We have presented new MUSE observations targeting the edge of the H I disc in the nearby edge-on galaxy UGC 7321. An emission line is detected in a deep 5.7-h exposure at $\lambda \sim 6574$ Å, which is the wavelength where Hα is expected given the H I radial velocity of UGC 7321. The emission line is also spatially resolved in narrow band images reconstructed from the MUSE data cube. The detected signal is located in close proximity of the edge of the MUSE FOV, and it lies in the wing of a sky line at $\lambda \sim 6577$ Å. Combined, these effects introduce a substantial uncertainty that dominates the error budget of our measurement.

Despite these additional sources of uncertainty, we have shown that an astrophysical signal is consistently recovered within data cubes reduced with different pipelines, and within data cubes containing two independent sets of exposures. Further, through the study of mock data cubes, we have shown that the detected emission line has properties consistent with that expected from an astrophysical signal associated with UGC 7321. Altogether, we conclude that we have detected Hα recombination from the edge of the H I disc of UGC 7321 with a line SB of $(1.2 \pm 0.1 \pm 0.5) \times 10^{-19}$ erg s^{-1} cm^{-2} arcsec^{-2}. Here, the first error indicates the statistical uncertainty and the second error characterizes the presence of the additional sources of uncertainties discussed above.

We present new radiative transfer calculations that self-consistently solve for the ionization and temperature structure of an exponential disc. The joint analysis of spatially resolved H I column density and Hα SB maps enables us to translate the observed SB into a value for the H I photoionization rate of the UVB. Following this procedure, our current measurement implies $\Gamma_{\rm H I} \sim (6-8) \times 10^{-14}$ s^{-1}, which is in line with the values inferred from the statistics of the low-redshift Lyα forest. While it is quite

likely that Hα emission at the location of our observations is primarily driven by photoionization arising from the UVB, we caution that an unknown contamination from other sources of ionization may be present. Thus, we can only place a formal upper limit on the H I photoionization rate with current observations, but we consider this measurement at the edge of the H I disc as an estimate of the actual intensity of the ionizing UVB.

Despite the substantial systematic uncertainty that affects our measurement, our work has demonstrated the potential that future MUSE observations have in constraining the intensity of the UVB in the local Universe. Through a grid of radiative transfer calculations, we have shown how detailed Hα maps of the ionization front could be used jointly with H I maps to precisely constrain $\Gamma_{\rm H I}$. To achieve better measurements of the UVB intensity, future work should however address the following two limitations of the current analysis.

Observationally, better precision on the SB measurement is mandatory for improving constraints on the UVB photoionization rate. With the use of mock data, we have shown that a precision of ~ 5–10 per cent can be easily achieved with MUSE in regions close to the centre of the FOV and far from sky lines. Thus, thanks to improved predictions of the spatial location of the Hα emission in UGC 7321 (Fig. 10), MUSE follow-up observations are expected to sample more accurately the location of the ionization front. Also, by observing the east side of the galaxy with a radial velocity of ~ 300–400 km s^{-1}, the Hα emission line shifts to ~ 6570 Å, in a region away from sky lines. Thus, measurements with errors below ~ 5–10 per cent should be possible in the near future.

As the precision of observations improves, models should be refined to reliably convert the observed SB into a measurement for the H I photoionization rate. The primary effect that should be accounted for in future analyses is the impact of local sources of

ionization. Models that include only the effects of the UVB predict a characteristic shape of the Hα emission (Fig. 9) that can be used to test whether the edge of the disc is illuminated by an external radiation field or whether local sources contribute significantly. Ancillary multiwavelength observations for the star-forming disc of UGC 7321 should be used to constrain the spectral energy distribution of local sources that can be added as further contribution to the ionization budget in radiative transfer models. Additional improvements include the treatment of metals and dust in a full three-dimensional radiative transfer calculation.

To further obviate to the problem of local sources, MUSE observations can target 'dark' clouds, where prominent star formation is absent. This experiment has been already attempted, for instance, targeting the intergalactic cloud H I 1225+01 (e.g. Vogel et al. 1995; Weymann et al. 2001). Deep MUSE observations will be able to further improve on current limits on the Hα SB, reaching levels of $\sim 10^{-20}$ erg s^{-1} cm^{-2} arcsec^{-2}. Future experiments could also search for the population of 'RELHICs', which are dark and gas-rich haloes that are predicted in Λ cold dark matter simulations (e.g. Sternberg, McKee & Wolfire 2002; Davies et al. 2006; Benítez-Llambay et al. 2017). Given the simple physics that regulates the properties of these dark galaxies, accurate measurements of the UVB intensity should be possible with deep MUSE follow-up observations.

From our analysis and from these considerations, we conclude that new measurements of the UVB intensity at $z \sim 0$ via Hα fluorescence appear within reach in the era of large format integral field spectrographs at 8 m class telescopes.

ACKNOWLEDGEMENTS

REFERENCES

Adams J. J., Uson J. M., Hill G. J., MacQueen P. J., 2011, ApJ, 728, 107
Alam S. et al., 2015, ApJS, 219, 12
Astropy Collaboration et al., 2013, A&A, 558, A33
Bacon R. et al., 2010, in McLean I. S., Ramsay S. K., Takami H., eds, Proc. SPIE Conf. Ser. Vol. 7735, Ground-Based and Airborne Instrumentation for Astronomy III. SPIE, Bellingham, p. 773509
Bajtlik S., Duncan R. C., Ostriker J. P., 1988, ApJ, 327, 570
Becker G. D., Bolton J. S., 2013, MNRAS, 436, 1023
Benítez-Llambay A. et al., 2017, MNRAS, 465, 3913
Bertin E., Arnouts S., 1996, A&AS, 117, 393
Bland-Hawthorn J., Freeman K. C., Quinn P. J., 1997, ApJ, 490, 143
Bolton J. S., Haehnelt M. G., 2007, MNRAS, 382, 325
Bolton J. S., Haehnelt M. G., Viel M., Springel V., 2005, MNRAS, 357, 1178
Borisova E., Cantalupo S., Lilly S. J. et al., 2016, ApJ, 831, 39
Bunker A. J., Marleau F. R., Graham J. R., 1998, AJ, 116, 2086
Calzetti D., Harris J., Gallagher J. S., III, Smith D. A., Conselice C. J., Homeier N., Kewley L., 2004, AJ, 127, 1405
Cantalupo S., Porciani C., Lilly S. J., Miniati F., 2005, ApJ, 628, 61
Ćirković M. M., Bland-Hawthorn J., Samurović S., 1999, MNRAS, 306, L15
Cristiani S., Serrano L. M., Fontanot F., Vanzella E., Monaco P., 2016, MNRAS, 462, 2478
Davies J. I., Disney M. J., Minchin R. F., Auld R., Smith R., 2006, MNRAS, 368, 1479
Donahue M., Aldering G., Stocke J. T., 1995, ApJL, 450, L45
Dove J. B., Shull J. M., 1994, ApJ, 423, 196
Faucher-Giguère C.-A., Lidz A., Zaldarriaga M., Hernquist L., 2008a, ApJ, 673, 39
Faucher-Giguère C.-A., Lidz A., Hernquist L., Zaldarriaga M., 2008b, ApJ, 688, 85
Faucher-Giguère C.-A., Lidz A., Zaldarriaga M., Hernquist L., 2009, ApJ, 703, 1416
Fumagalli M., Cantalupo S., Dekel A., Morris S. L., O'Meara J. M., Prochaska J. X., Theuns T., 2016, MNRAS, 462, 1978
Gaikwad P., Srianand R., Choudhury T. R., Khaire V., 2016, preprint (arXiv:1610.06572)
Gould A., Weinberg D. H., 1996, ApJ, 468, 462
Gunn J. E., Peterson B. A., 1965, ApJ, 142, 1633
Haardt F., Madau P., 1996, ApJ, 461, 20
Haardt F., Madau P., 2001, in Neumann D.M., Van J.T.T., eds, Clusters of Galaxies and the High Redshift Universe Observed in X-rays. Available at: https://books.google.co.uk/books/about/Clusters_of_Galaxies_and_the_High_Redshi.html?id=NFMhtwAACAAJ
Haardt F., Madau P., 2012, ApJ, 746, 125
Hoopes C. G., Walterbos R. A. M., 2003, ApJ, 586, 902
Karachentsev I. D., Kaisina E. I., 2013, AJ, 146, 46
Khaire V., Srianand R., 2015, MNRAS, 451, L30
Kollmeier J. A. et al., 2014, ApJ, 789, L32
Leitherer C. et al., 1999, ApJS, 123, 3
Madau P., Haardt F., 2015, ApJ, 813, L8
Madsen G. J., Reynolds R. J., Haffner L. M., Tufte S. L., Maloney P. R., 2001, ApJ, 560, L135
Maloney P., 1993, ApJ, 414, 41
Matthews L. D., Gallagher J. S., III, van Driel W., 1999, AJ, 118, 2751
Murdoch H. S., Hunstead R. W., Pettini M., Blades J. C., 1986, ApJ, 309, 19
Oey M. S. et al., 2007, ApJ, 661, 801
Okamoto T., Gao L., Theuns T., 2008, MNRAS, 390, 920
Oñorbe J., Hennawi J. F., Lukić Z., 2016, preprint (arXiv:1607.04218)
Pequignot D., Petitjean P., Boisson C., 1991, A&A, 251, 680
Prochaska J. X. et al., 2013, ApJ, 776, 136
Rauch M. et al., 1997, ApJ, 489, 7
Rauch M. et al., 2008, ApJ, 681, 856
Rollinde E., Srianand R., Theuns T., Petitjean P., Chand H., 2005, MNRAS, 361, 1015
Schaye J., 2006, ApJ, 643, 59
Schlafly E. F., Finkbeiner D. P., 2011, ApJ, 737, 103
Shull J. M., Roberts D., Giroux M. L., Penton S. V., Fardal M. A., 1999, AJ, 118, 1450
Shull J. M., Moloney J., Danforth C. W., Tilton E. M., 2015, ApJ, 811, 3
Soto K. T., Lilly S. J., Bacon R., Richard J., Conseil S., 2016, MNRAS, 458, 3210
Sternberg A., McKee C. F., Wolfire M. G., 2002, ApJS, 143, 419

Theuns T., Schaye J., Zaroubi S., Kim T.-S., Tzanavaris P., Carswell B., 2002, ApJ, 567, L103

Uson J. M., Matthews L. D., 2003, AJ, 125, 2455

Uson J. M., Adams J. J., Hill G. J., MacQueen P. J., 2012, BAAS, 219, 312.01

Verner D. A., Ferland G. J., Korista K. T., Yakovlev D. G., 1996, ApJ, 465, 487

Viel M., Haehnelt M. G., Bolton J. S., Kim T.-S., Puchwein E., Nasir F., Wakker B. P., 2016, preprint (arXiv:1610.02046)

Vogel S. N., Weymann R., Rauch M., Hamilton T., 1995, ApJ, 441, 162

Voges E. S., Walterbos R. A. M., 2006, ApJ, 644, L29

Weilbacher P. M., Streicher O., Urrutia T., Pécontal-Rousset A., Jarno A., Bacon R., 2014, ASP Conf. Ser. Vol. 485, Astronomical Data Analysis Software and Systems XXIII. Astron. Soc. Pac., San Francisco, p. 451

Weymann R. J., Vogel S. N., Veilleux S., Epps H. W., 2001, ApJ, 561, 559

This paper has been typeset from a TEX/LATEX file prepared by the author.